Effects of redox mediators on α-Fe$_2$O$_3$ exposed by {012} and {104} facets for photocatalytic water oxidation

Yu Lei Wang, Yu Hang Li, Xue Lu Wang, Yu Hou, Ai Ping Chen*, Hua Gui Yang*

Key Laboratory for Ultrafine Materials of Ministry of Education, School of Materials Science and Engineering, East China University of Science and Technology, 130 Meilong Road, Shanghai 200237, China

ARTICLE INFO

ABSTRACT

The mechanism study of redox mediator to transfer the photogenerated electrons is extremely desirable for artificial Z-scheme photocatalytic systems. Here we find that the α-Fe$_2$O$_3$ exposed by {012} and {104} facets can facilitate the reduction of IO$_3^-$, which results in increasing the activity of photocatalytic water oxidation significantly. By employing NaIO$_3$ as an electron acceptor, the O$_2$ evolution activity (309.4 μmol h^{-1} g^{-1}) of α-Fe$_2$O$_3$ photocatalyst mainly exposed by {012} and {104} facets is 84 times higher than that (3.68 μmol h^{-1} g^{-1}) of α-Fe$_2$O$_3$ mostly exposed by {101} and {111} planes. We anticipate that the findings in this work may open the door for further development of enhanced Z-scheme photocatalytic systems.

1. Introduction

Photocatalytic water splitting into hydrogen (H$_2$) and oxygen (O$_2$) has been regarded as a promising means of storing solar energy [1,2]. In the past three decades, the artificial heterogeneous Z-scheme photocatalytic systems for water splitting have been extensively investigated [3,4]. This system features the unique electron transfer, which is fully dependent on the redox reactions of the electron acceptor/donor pair. The electron acceptor is reduced into the electron donor in the conduction band of the O$_2$-evolving photocatalyst and the electron donor is oxidized into the electron acceptor in the valence band of H$_2$-evolving photocatalyst, respectively [5]. Unfortunately, it is often difficult to control the migration of electrons from the O$_2$-evolving photocatalyst to the H$_2$-evolving photocatalyst sufficiently, which results in low efficiency of the reported Z-scheme photocatalytic systems [6]. Thus, the mechanism study of the redox mediators for efficient photogenerated electrons transfer is extremely desirable.

Noteworthily, the properties of the solid-liquid contact interface between the photocatalysts and redox reagent determine the rate of electron transfer in Z-scheme photocatalytic systems. As an electron acceptor/donor pair, the IO$_3^-$/I$^-$ redox reagent has been widely used in the Z-scheme photocatalytic systems [7–9]. However, since the water oxidation reaction is a bottleneck of water splitting owed to the four-electron process, it could be more challenging in Z-scheme photocatalytic system when the redox mediators (e.g., IO$_3^-$/I$^-$) are used [10,11]. Therefore, the search for suitable semiconductors as O$_2$-evolving photocatalysts that promote the reduction of IO$_3^-$ is of great importance to enhance the performance of corresponding Z-scheme photocatalytic systems.

We have reported preliminary results in the electrocatalytic process of redox mediators [12], which has attracted considerable interests for its wide range of applications in other areas, for example the Z-scheme photocatalytic systems for water splitting. Herein, for the first time, we study the effects of redox reagent on the activity of O$_2$ evolution over α-Fe$_2$O$_3$ nanocrystals exposed by different facets. The O$_2$ evolution activity of α-Fe$_2$O$_3$ photocatalyst mostly exposed by {012} and {104} facets is 84 times higher than that of α-Fe$_2$O$_3$ mostly exposed by {101} and {111} planes in NaIO$_3$ aqueous solution. Moreover, we explore a series of low-cost O$_2$-evolving photocatalysts, and successfully confirm that α-Fe$_2$O$_3$ nanocrystals mainly bounded by (012) and (104) facets demonstrate remarkable photocatalytic activity of O$_2$ evolution in the presence of a sacrificial electron acceptor IO$_3^-$. The findings indicate that the α-Fe$_2$O$_3$ mentioned above could act as a promising candidate of O$_2$-evolving photocatalyst for designing a prominent Z-scheme photocatalytic system.

* Corresponding authors.
E-mail addresses: apchen@ecust.edu.cn (A.P. Chen), hgyang@ecust.edu.cn (H.G. Yang).
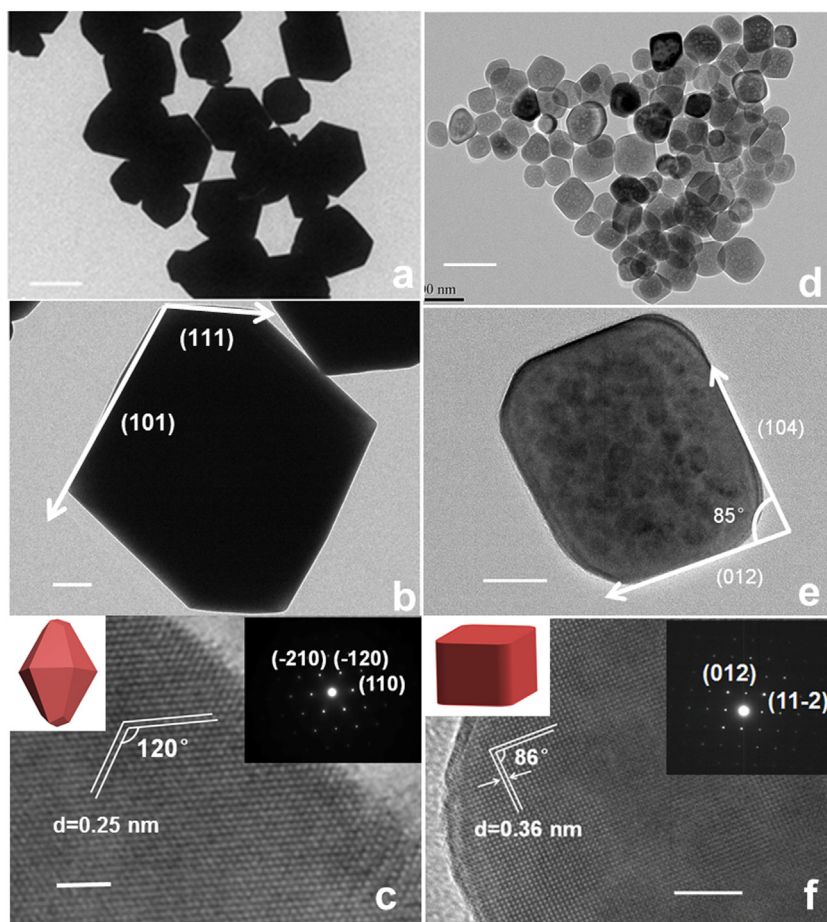
Fig. 1. (HR)TEM images of Octo-Fe$_2$O$_3$ crystals (a–c) and Cubic-Fe$_2$O$_3$ particles (d–f). The corresponding SAED patterns are shown in the inset. The scale bars in panels (a–f) are 1 μm, 200 nm, 2 nm, 100 nm, 20 nm and 5 nm, respectively. Cubic-Fe$_2$O$_3$: cube-like α-Fe$_2$O$_3$; Octo-Fe$_2$O$_3$: octodecahedron α-Fe$_2$O$_3$.

2. Results

The α-Fe$_2$O$_3$ nanocrystals mainly bounded by {101} and {111} planes were synthesized via a one-step hydrothermal process using sodium fluoride as the reaction controlling agent [13,14]. The morphology and structure details of the synthesized α-Fe$_2$O$_3$ samples were investigated by scanning electron microscope (SEM) and transmission electron microscopy (TEM) measurements. SEM and TEM images (Fig. S1a and Fig. 1a–c) of the obtained samples α-Fe$_2$O$_3$ display octodecahedron crystals enclosed by twelve (101) planes and six (111) planes [13,14]. A high-resolution TEM (HRTEM) image (Fig. 1c) and selected area electron diffraction (SAED, inset in Fig. 1c) of octodecahedron α-Fe$_2$O$_3$ (Octo-Fe$_2$O$_3$) exhibit two sets of lattice fringes both to be 0.25 nm, which can be assigned to the lattice fringe of (110), (−210) and (−120) planes of α-Fe$_2$O$_3$ crystal structure [13,15]. Moreover, the angle of 120° between these two lattice fringes is consistent with the angle of the (110) and (−210) planes [13,15].

For the synthesis of the other kind of α-Fe$_2$O$_3$ nanocrystals mainly exposed by {012} and {104} facets, concentrated sodium-hydroxide aqueous solution was used as the reaction controlling agent [12,16]. As shown in high-magnification SEM image (Fig. S1b), the synthesized nanocrystals are cube-like particles with nonuniform sizes. We further carried out the TEM and HRTEM characterization to investigate the inner crystal structures of cube-like α-Fe$_2$O$_3$ (Cubic-Fe$_2$O$_3$). In Fig. 1d and e, the as-prepared crystals exhibit cube-like profiles with sizes ranging from 30 to 70 nm, which is in agreement with the SEM results. The HRTEM image (Fig. 1e) reveals two groups of (012) and (104) planes with one

interfacial angle that is approximately 85° [12,17]. Fig. 1f exhibits the lattice spacing of 0.36 nm, which can be assigned to the {012} crystal plane of α-Fe$_2$O$_3$ [15]. A close look at this cube demonstrates that one dihedral angle between adjacent lateral facets is 86° [15,17]. Similar results could be obtained from the selected area electron diffraction pattern (in the inset). These results suggest that the Cubic-Fe$_2$O$_3$ nanocrystals are single crystals, dominated by exposing {012} and {104} facets.

Powder X-ray diffraction (XRD, Fig. 2a) confirms that all diffraction peaks of the synthesized samples are agree with the crystal structure of the α-Fe$_2$O$_3$ phase (JCPDS No. 84-0310) [12]. Further, the bandgap calculations of the obtained Cubic-Fe$_2$O$_3$ and Octo-Fe$_2$O$_3$ samples are worth noting. UV–vis diffuse reflectance spectra (Fig. 2b) show that the Cubic-Fe$_2$O$_3$ and Octo-Fe$_2$O$_3$ samples have similar absorption edge around 730 nm, indicating that both of them display a remarkable visible-light-harvesting ability. The band gap of Cubic-Fe$_2$O$_3$ and Octo-Fe$_2$O$_3$ samples are determined from the Tauc plot [1]. The figure (inset) displays a good linear fit when using r = 1/2, claiming the indirect band gap of Cubic-Fe$_2$O$_3$ and Octo-Fe$_2$O$_3$ samples are 1.69 and 1.68 eV, respectively [18]. The valence band of Cubic-Fe$_2$O$_3$ and Octo-Fe$_2$O$_3$ nanocrystals were also measured by valence band X-ray photoelectron spectroscopy (XPS) with the edge of the maximum energy at about 2.8 and 2.6 eV, respectively (Fig. 2c). Combined with the results of the above-measured band gap and valence band, the energy band diagram of Cubic-Fe$_2$O$_3$ and Octo-Fe$_2$O$_3$ nanocrystals were shown in Fig. 2d. The electrode potential of Cubic-Fe$_2$O$_3$ and Octo-Fe$_2$O$_3$ samples are not negative than the redox potential of H$^+$/H$_2$ (0 V vs. NHE), which indicates that they cannot split water to release H$_2$.
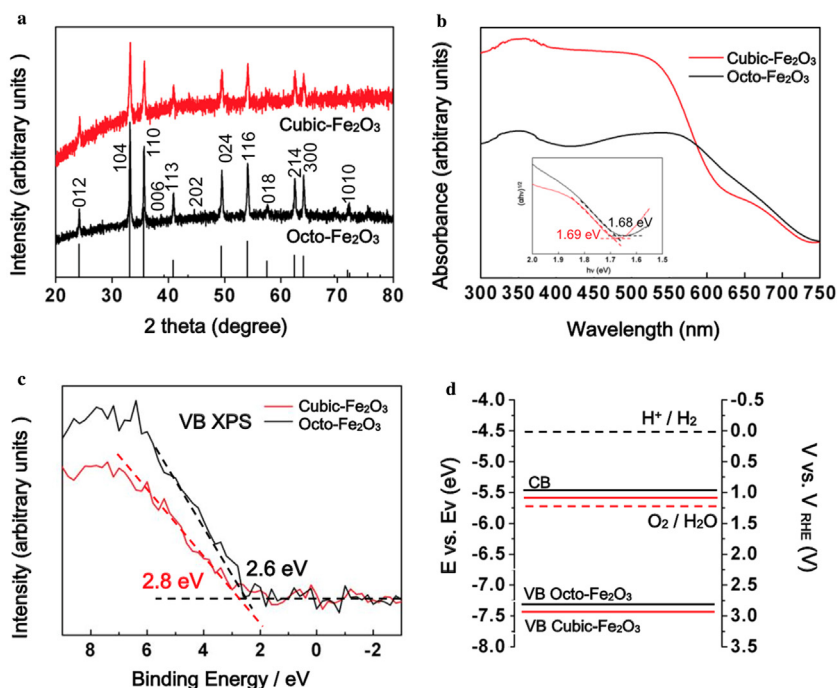
Fig. 2. (a) XRD patterns of the samples Cubic-Fe$_2$O$_3$ and Octo-Fe$_2$O$_3$. (b) UV–vis diffuse reflectance spectra of the samples Cubic-Fe$_2$O$_3$ and Octo-Fe$_2$O$_3$; Inset: $(\alpha h\nu)^{1/2}$ versus hν curves of Cubic-Fe$_2$O$_3$ and Octo-Fe$_2$O$_3$. The horizontal dashed black and white lines mark the baselines; the other dashed lines are the tangent of the curves. The intersection values are the band gaps. (c) Valence-band XPS spectra of the samples Cubic-Fe$_2$O$_3$ and Octo-Fe$_2$O$_3$. (d) Band structure diagram for Cubic-Fe$_2$O$_3$ and Octo-Fe$_2$O$_3$ photocatalysts. VB, valence band; CB, conduction band. Cubic-Fe$_2$O$_3$ (white line): cube-like α-Fe$_2$O$_3$; Octo-Fe$_2$O$_3$ (black line): octodecahedron α-Fe$_2$O$_3$.

However, the valence band level of Cubic-Fe$_2$O$_3$ and Octo-Fe$_2$O$_3$ are more positive than the redox potential of O$_2$/H$_2$O (1.23 V), suggesting the thermodynamic feasibility for water oxidation [19–21].

To investigate the effects of redox reagent on the activities of O$_2$ evolution over the as-prepared α-Fe$_2$O$_3$ nanocrystals mainly bounded by different facets, the photocatalytic O$_2$ evolution over Cubic-Fe$_2$O$_3$ and Octo-Fe$_2$O$_3$ samples in the presence of the sacrificial reagent sodium iodate (NaIO$_3$) under UV–vis irradiation ($\lambda > 300$ nm) was therefore tested (Fig. 3a). It was found that the O$_2$ evolution rate of Cubic-Fe$_2$O$_3$ photocatalyst mainly exposed by {012} and {104} facets in an aqueous NaIO$_3$ solution (9.28 μmol h^{-1}) was 84 times higher than that of Octo-Fe$_2$O$_3$ mostly exposed by {101} and {111} planes (0.11 μmol h^{-1}), indicating that the photogenerated electrons transfer more effectively in the former. It is considered that the reaction mechanism in the presence of IO$_3^-$ as sacrificial reagent can be described as follow [22–25]:

$$IO_{3^-} + 3H_2O + 6e^- \rightarrow I^- + 6OH^- \tag{1}$$
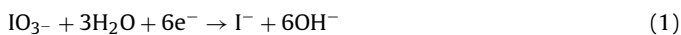
The reaction of iodine reduction (step I) occurring at the liquid–solid interface would promote water oxidation. Noteworthily, we previously reported that Fe$_2$O$_3$(012) and Fe$_2$O$_3$(104) exhibit kinetically good performance for iodine reduction [12]. Therefore, the as-prepared Cubic-Fe$_2$O$_3$ nanocrystals demonstrate remarkable photocatalytic activity of O$_2$ evolution because of its capacity for the reduction of IO$_3^-$.

Moreover, the O$_2$ generation tests of Co$_3$O$_4$, MnO$_2$ and CeO$_2$ were compared with synthesized α-Fe$_2$O$_3$ (as shown in Fig. 3b). It can be seen that the compounds MnO$_2$, CeO$_2$ or Co$_3$O$_4$ is less active than Cubic-Fe$_2$O$_3$ for O$_2$ evolution. The apparent quantum efficiency measurement shows that the quantum yield of as-prepared Cubic-Fe$_2$O$_3$ is around 4.0% at 365 nm. Furthermore, the visible-light-driven oxygen generation of synthesized Cubic-Fe$_2$O$_3$ was investigated (Fig. 3c). When $\lambda > 420$ nm, continuous O$_2$ evolution without noticeable decrease was observed throughout the

photocatalytic cycling (10$\times$) experiments with intermittent evacuation every 2 h, indicating it functions as a stable photocatalyst for O$_2$ evolution in water splitting. The average oxygen evolution rate of the synthesized Cubic-Fe$_2$O$_3$ reaches to 4.3 μmol h^{-1} g^{-1}, with an apparent quantum yield of 0.02% at 420 nm. Therefore, the as-prepared Cubic-Fe$_2$O$_3$ could be a promising candidate of O$_2$-evolving photocatalyst for designing a prominent Z-scheme photocatalytic system.

It is worthwhile discussing the origin of excellent activity of O$_2$ evolution for the as-prepared Cubic-Fe$_2$O$_3$. It is known that H$_2$O is oxidized to O$_2$ on surface reaction sites of photocatalyst [21]. Fortunately, the reaction of iodine reduction occurs at the liquid–solid interface between redox reagent and α-Fe$_2$O$_3$. Therefore, we performed the technique of electrochemical impedance spectroscopy (EIS) to study interfacial carrier transfer. Fig. 4a and Fig. 4b compare the Nyquist plots of Cubic-Fe$_2$O$_3$ and Octo-Fe$_2$O$_3$ samples. When moving across the solid–liquid interface, the carrier transfer resistance of Cubic-Fe$_2$O$_3$ is small than that of Octo-Fe$_2$O$_3$ in the electrolyte of 0.5 M Na$_2$SO$_4$ water solution. Moreover, the radius of the semicircle of Cubic-Fe$_2$O$_3$ is obviously smaller than that of Octo-Fe$_2$O$_3$ in the electrolyte of 0.5 M NaIO$_3$ water solution, indicating that the as-prepared Cubic-Fe$_2$O$_3$ facilitates the reaction of iodine reduction occurring at the liquid–solid interface. In addition, the carrier transfer resistance of Cubic-Fe$_2$O$_3$ in NaIO$_3$ water solution shows smaller than that in Na$_2$SO$_4$ water solution, which may result from more charge carriers participating the reaction of iodine reduction in the former [26]. Considering that the Cubic-Fe$_2$O$_3$ sample facilitates the reaction of iodine reduction (Fig. 4c and d) [12], more photogenerated electrons and holes on the surface participate in reactions, and the activity of O$_2$ evolution over the as-prepared α-Fe$_2$O$_3$ nanocrystals increases significantly in the presence of the electron acceptor IO$_3^-$. In this work, we improved the O$_2$ generation rate of α-Fe$_2$O$_3$ sample and illustrated one of the issues affecting the reaction of iodine reduction.
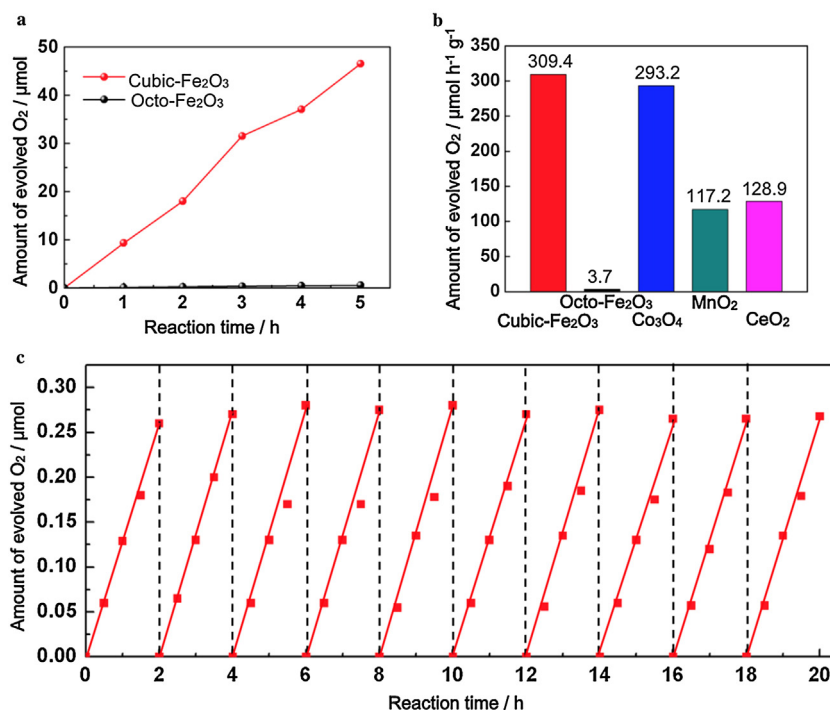
Fig. 3. (a) Photocatalytic O_2 evolution from samples Cubic-Fe$_2$O$_3$ and Octo-Fe$_2$O$_3$ in a 20 mM NaIO$_3$ and 10 mM Na$_3$PO$_4$·12H$_2$O aqueous solution. (b) Rates of O_2 evolution over various metal oxide in a 20 mM NaIO$_3$ and 10 mM Na$_3$PO$_4$·12H$_2$O aqueous solution. (c) Photocatalytic O_2 evolution from Cubic-Fe$_2$O$_3$ under visible light irradiation. Cubic-Fe$_2$O$_3$: cube-like α-Fe$_2$O$_3$; Octo-Fe$_2$O$_3$: octodecahedron α-Fe$_2$O$_3$.
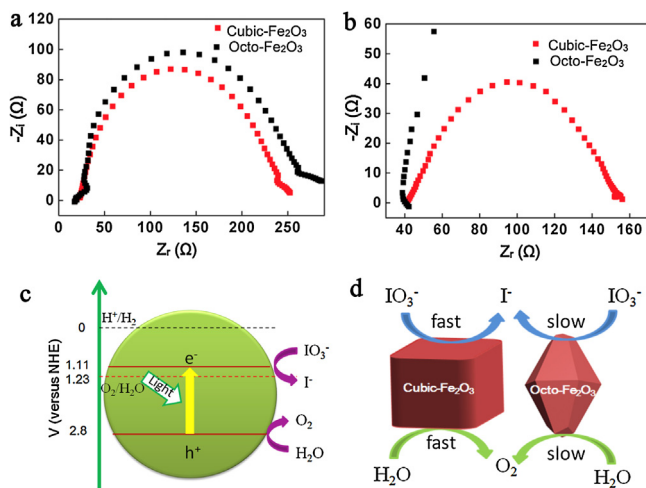
Fig. 4. Comparison of the Nyquist plots of the Cubic-Fe$_2$O$_3$ and Octo-Fe$_2$O$_3$ catalysts. The electrolyte is 0.5 M Na$_2$SO$_4$ water solution (a) or 0.5 M NaIO$_3$ water solution (b). (c) Schematic drawing of redox potentials of Cubic-Fe$_2$O$_3$. (d) Schematic drawing of the reaction. Cubic-Fe$_2$O$_3$: cube-like α-Fe$_2$O$_3$; Octo-Fe$_2$O$_3$: octodecahedron α-Fe$_2$O$_3$.

3. Conclusion

In conclusion, we found that α-Fe$_2$O$_3$ mainly exposed by {012} and {104} facets can facilitate the reaction of iodine reduction occurring at the liquid–solid interface between redox reagent and α-Fe$_2$O$_3$. As a result, the availability of photogenerated carriers can be promoted originating from inhibiting the recombination of photogenerated electrons and holes on the surface. Meanwhile, the photocatalytic O_2 evolution rate of as-prepared α-Fe$_2$O$_3$ sample was enhanced to 309.4 μmol h^{-1} g^{-1}, compared with that (3.7 μmol h^{-1} g^{-1}) of α-Fe$_2$O$_3$ mostly exposed by {101} and {111}

planes. The results presented here provide new insights into the construction more prominent Z-scheme photocatalytic systems.

Appendix A. Supplementary data

Supplementary data associated with this article can be found, in the online version, at http://dx.doi.org/10.1016/j.apcatb.2016.11.028.

References

[1] J. Liu, Y. Liu, N. Liu, Y. Han, X. Zhang, H. Huang, Y. Lifshitz, S.T. Lee, J. Zhong, Z. Kang, Science 347 (2015) 970–974.
[2] L. Liao, Q. Zhang, Z. Su, Z. Zhao, Y. Wang, Y. Li, X. Lu, D. Wei, G. Feng, Q. Yu, X. Cai, J. Zhao, Z. Ren, H. Fang, F. Robles-Hernandez, S. Baldelli, J. Bao, Nat. Nanotechnol. 9 (2014) 69–73.
[3] R. Niishiroa, S. Tanakaa, A. Kudo, Appl. Catal. B-Environ. 150 (2014) 187–196.
[4] H.J. Yun, H. Lee, N.D. Kim, D.M. Lee, S. Yu, J. Yi, ACS Nano 5 (2011) 4084–4090.
[5] P. Zhou, J. Yu, M. Jaroniec, Adv. Mater. 26 (2014) 4920–4935.
[6] K. Sekizawa, K. Maeda, K. Domen, K. Koike, O. Ishitani, J. Am. Chem. Soc. 135 (2013) 4596–4599.
[7] Y. Miseki, S. Fujiyoshi, T. Gunjib, K. Sayama, Catal. Sci. Technol. 3 (2013) 1750–1756.
[8] S. Chen, Y. Qi, T. Hisatomi, Q. Ding, T. Asai, Z. Li, S.S.K. Ma, F. Zhang, K. Domen, C. Li, Angew Chem. Int. Ed. 54 (2015) 8498–8501.
[9] Q. Wang, T. Hisatomi, S.S.K. Ma, Y. Li, K. Domen, Chem. Mater. 26 (2014) 4144–4150.
[10] M. Tabata, K. Maeda, M. Higashi, D. Lu, T. Takata, R. Abe, K. Domen, Langmuir 26 (2010) 9161–9165.

[11] C.G. Silva, Y. Bouizi, V. Fornes, H. Garcia, J. Am. Chem. Soc. 131 (2009) 13833–13839.
[12] Y. Hou, D. Wang, X.H. Yang, W.Q. Fang, B. Zhang, H.F. Wang, G.Z. Lu, P. Hu, H.J. Zhao, H.G. Yang, Nat. Commun. 4 (2013) 1583.
[13] C.W. Wang, S. Yang, W.Q. Fang, P. Liu, H. Zhao, H.G. Yang, Nano Lett. 16 (2016) 427–433.
[14] B.B. Lv, Z. Liu, H. Tian, Y. Xu, D. Wu, Y. Sun, Adv. Funct. Mater. 20 (2010) 3987–3996.
[15] X. Zhou, J. Lan, G. Liu, K. Deng, Y. Yang, G. Nie, J. Yu, L. Zhi, Angew. Chem. Int. Ed. 51 (2012) 178–182.
[16] M. Žic, M. Ristić, S. Musić, J. Mol. Struct. 993 (2011) 115–119.
[17] J. Yin, Z. Yu, F. Gao, J. Wang, H. Pang, Q. Lu, Angew. Chem. Int. Ed. 122 (2010) 6472–6476.
[18] T.K. Townsend, E.M. Sabio, N.D. Browning, F.E. Osterloh, Energy Environ. Sci. 4 (2011) 4270–4275.
[19] X. Chen, L. Liu, P.Y. Yu, S.S. Mao, Science 331 (2011) 746–750.
[20] Z. Yi, J. Ye, N. Kikugawa, T. Kako, S. Ouyang, H. Stuart-Williams, H. Yang, J. Cao, W. Luo, Z. Li, Y. Liu, R.L. Withers, Nat. Mater. (2010) 559–564.
[21] A. Kudo, Y. Miseki, Chem. Soc. Rev. 38 (2009) 253–278.
[22] K. Sayama, K. Mukasa, R. Abe, Y. Abe, H. Arakawa, J. Photoch. Photobio. A 148 (2002) 71–77.
[23] K. Maeda, D. Lu, K. Domen, ACS Catal. 3 (2013) 1026–1033.
[24] L. Schwertmann, A. Grünert, A. Pougin, C. Sun, M. Wark, R. Marschall, Adv. Funct. Mater. 10 (2014) 905–912.
[25] Y. Inoue, Energy Environ. Sci. 2 (2009) 364–386.
[26] Z. Lin, J. Xiao, L. Li, P. Liu, C. Wang, G. Yang, Adv. Energy Mater. 6 (2016) 1501865.